Metrol. Meas. Syst., Vol. 28 (2021) No. 2, pp. 289–305
DOI: 10.24425/mms.2021.136608

PAN POLSKA AKADEMIA NAUK

METROLOGY AND MEASUREMENT SYSTEMS
Index 330930, ISSN 0860-8229
www.metrology.wat.edu.pl

M&MS

QUASI-DISTRIBUTED NETWORK OF LOW-COHERENCE FIBER-OPTIC FABRY–PÉROT SENSORS WITH CAVITY LENGTH-BASED ADDRESSING

Katarzyna Karpienko, Marcin J. Marzejon, Adam Mazikowski, Jerzy Pluciński

Gdańsk University of Technology, Faculty of Electronics, Telecommunications and Informatics, Department of Metrology and Optoelectronics, 11/12 Gabriela Narutowicza St., 80-233 Gdańsk, Poland (*katkarip@pg.edu.pl*, +48 58 347 1584, ✉ *marcin.marzejon@pg.edu.pl*, *adamazik@pg.edu.pl*, *jerpluc@pg.edu.pl*)

Abstract

Distributed measurement often relies on sensor networks. In this paper, we present the construction of low-coherence fiber-optic Fabry–Pérot sensors connected into a quasi-distributed network. We discuss the mechanism of spectrum modulation in this type of sensor and the constraints of assembly of such sensors in the network. Particular attention was paid to separate the signals from individual sensors which can be achieved by cavity length-based addressing. We designed and built a laboratory model of a temperature sensors network. The employed sensors are low-coherence Fabry–Pérot interferometric sensors in a fiber-optics configuration. The extrinsic sensor cavity utilizes the thermal expansion of ceramics, and the sensors are addressed by the different lengths of the cavities. The obtained test results show that the signal components from each sensor can be successfully separated, and the number of sensors could be expanded depending on the FWHM of the light source.

Keywords: Fabry–Pérot interferometer, sensors network, fiber-optics sensor, interferometry.

1. Introduction

Over the years, *fiber-optics sensors* (FOSs) have been employed in many metrological applications. They enable precise and high-resolution measurements of various physical quantities, among others: refractive index [1–3], displacement [4, 5], vibration [6, 7], strain [8, 9], pressure [10], temperature [11, 12], humidity [13], magnetic field [14], liquid level [15], and concentration of liquids [16]. In the very basic configuration, a FOS contains a light source, an optical fiber, a modulator, and a detection system [17]. Such a sensor uses the modulation of the light propagated in the fiber or an element of the fiber-optic path, to encode the information about the measurand.

Fiber-optics sensors are versatile in their applications. Both point and distributed measurements can be performed using FOSs, as well as quasi-distributed measurements when many of them are connected into a network [18–21]. FOSs are very small in size – the diameter of stan-

Article history: received September 7, 2020; revised November 10, 2020; accepted December 19, 2020; available online March 19, 2021.

dard single-mode fiber is 125 μm. Also, they can be used for even very remote measurements. In such operation mode, the measurement signal is provided directly to the receiving system without conversion to an electrical signal, giving another advantage which is lack risk of electric discharge. It enables applications for normally inaccessible areas and harsh environments, for instance, flammable substances extraction areas [19, 20].

The very common limitation of fiber-optic sensors-based measurement systems is the noise caused by time changes of the fiber-optics attenuation. This limitation can be overcome only for the particular types of FOSs. One of them are sensors for which the measurand changes the spectrum of the signal. Examples of such sensors are low-coherence fiber-optics sensors (LC-FOS) for which the interference causes a change of the signal spectrum. Besides the ability of to analyze the signal in the spectrum domain, LC-FOS can be easily miniaturized and applied in, *e.g.*, ultra-low-volume samples, or fast-changing parameters measurements dependent on the sensor time constant [22, 23].

The low-coherence fiber-optic sensors with a Fabry–Pérot cavity are well described in the literature and still explored for new applications and improved performance [24, 27]. There are reports about FOSs with Fabry–Pérot cavities made with nanosecond or femtosecond lasers [28, 29], lateral offset splicing [30], cavities created during the fiber splicing process [31], or using different types of fiber-optic, *e.g.* hollow core or microstructured optical fibers [5, 32]. For instance, in 2019, Marta Nespereira *et al.* proposed a refractive index sensor with a Fabry–Pérot cavity manufactured in standard single-mode telecommunication fiber using a nanosecond-pulse NIR Q-switched Nd:YAG laser [29]. In so prepared Fabry–Pérot cavity, its length was adjusted by a cleaver. For the proposed constructions, the sensor enables measurements with sensitivity up to 0.31 nm^{-1}/RIU using later analysis, or 54 dB/RIU using fringe visibility analysis. Another reported solution utilizes a capillary for in-fiber Fabry–Pérot cavity manufacturing [31]. So prepared strain sensor enables very-high sensitivity measurements (7.53 pm/$\mu\varepsilon$) for a cavity length of 2.189 μm. The main disadvantage of the mentioned solutions is the complicated and expensive process of Fabry–Pérot cavity manufacturing, requiring sophisticated equipment and training.

In this work, we proposed a low-coherence fiber-optic sensor with an extrinsic Fabry–Pérot cavity, placed at the end of the fiber and connected with a low-coherence measurement system. We chose this particular design because of, among others, the possibility of sensor miniaturization even down to hundreds of micrometers. In our solution, the standard SMF-28 optical fiber, or another type of fiber can be employed, which significantly decreases the time and cost of producing such a sensor. Moreover, sensors can be connected to form a network enabling simultaneous measurements at many points. The use of sensors with the Fabry–Pérot cavity operating in a sensor network is a new concept that requires a solution to the problem of addressing these sensors. The paper proposes a method of addressing them, which has been theoretically analyzed and tested experimentally. For a correctly designed sensor network, the proposed signal analysis enables to obtain separated signals from all sensors.

2. Low-coherence interferometric sensors with extrinsic Fabry–Pérot cavities

2.1. Principle of operation

The principle of operation of low-coherence interferometric sensors with extrinsic Fabry–Pérot cavities is based on measurement of the reflection (or transmission) spectrum of radiation propagated through or reflected from the cavity located at the end of the optical fiber. If the

Metrol. Meas. Syst., Vol. 28 (2021), No. 2, pp. 289–305
DOI: 10.24425/mms.2021.136608

measurand changes this spectrum (*e.g.* as a result of a change in the Fabry–Pérot cavity length or refractive index of the substance filling the cavity), then, by its analysis, the measurand value can be determined. Since the optical radiation reflected from the Fabry–Pérot cavity can be treated as the sum of many interfering beams coming out of the cavity, the amplitude spectral density at the sensor output is equal to the sum of the amplitude spectral density of individual beams, so the power spectral density $P_{\text{out}}(\lambda)$ of radiation at the output of the sensor can be determined as:

$$P_{\text{out}}(\lambda) = |U_{\text{out}}(\lambda)|^2 = \left| \sum_{i=0}^{\infty} U_i(\lambda) \right|^2, \tag{1}$$

where $U_{\text{out}}(\lambda)$ is amplitude spectral density of radiation reflected from the Fabry–Pérot cavity, $U_0(\lambda)$ is amplitude spectral density of radiation that reflected from the boundary surface between the end of optical fiber and the cavity, and $U_i(\lambda)$ (for $i > 0$) are the amplitude spectral densities of beams that propagated at the distance equal to $2iL$ inside the cavity (where L is the length of the cavity) and next were coupled to the optical fiber, and λ is the wavelength in a vacuum (note that the amplitude spectral densities $U_{\text{out}}(\lambda)$ and $U_i(\lambda)$ are complex functions and describe the radiation inside the optical fiber – see Fig. 1).

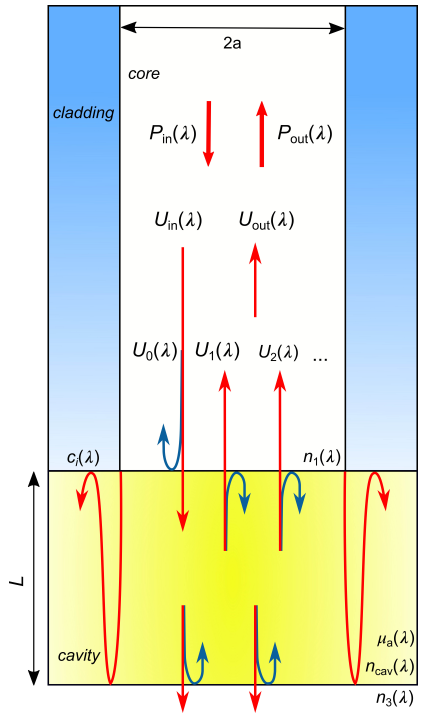

Fig. 1. Optical radiation propagating in the fiber-optic sensor with the extrinsic Fabry–Pérot cavity.

Contrary to classic Fabry–Pérot interferometers, which use interference of an infinite number of planar waves propagated between two parallel mirrors, fiber optic sensors with extrinsic Fabry–Pérot cavities use interference of an infinite number of non-planar waves derived from the beam outgoing from the end of the optical fiber. A detailed analysis of the operation of these sensors taking into account effects such as the diffraction phenomenon of the optical radiation beam inside

the cavity, the phase shift caused by the Gouy effect (the Gouy effect means an additional slight phase shift of the wave compared to a plane wave of the same frequency as the distance from the wave source increases; in the case of a Gaussian beam, this shift increases from zero to $\pi/2$ as the distance increases from zero to infinity from the beam waist), and the coupling coefficients $c_i(\lambda)$ of the waves from the cavity that are transmitted through the interface between the cavity and the core of the optical fiber is presented in [33, 34].

When the coefficient of reflection of the boundary surfaces between the optical fiber and the cavity or between the cavity and the center located behind the cavity is much smaller than 1, then the amplitude spectral densities $U_i(\lambda)$ for $i > 1$ are negligibly small (compared with $U_0(\lambda)$ or $U_1(\lambda)$) and then the dependence (1) will take the form

$$P_{\text{out}}(\lambda) = |U_0(\lambda) + U_1(\lambda)|^2 . \tag{2}$$

Amplitude spectral density $U_0(\lambda)$ can be determined directly from the Fresnel equation describing the ratio of reflected wave amplitude spectral density to the incident wave amplitude spectral density at the boundary of two media:

$$U_0(\lambda) = r_{12}(\lambda)U_{\text{in}}(\lambda), \tag{3}$$

where $U_{in}(\lambda)$ is the amplitude spectral density of the incident beam at the Fabry–Pérot cavity, $r_{12}(\lambda)$ is the complex amplitude reflectance at the interface between the optical fiber and the cavity:

$$r_{12}(\lambda) = \frac{n_1(\lambda) - n_{\text{cav}}(\lambda)}{n_1(\lambda) + n_{\text{cav}}(\lambda)}, \tag{4}$$

and $n_1(\lambda)$ and $n_{\text{cav}}(\lambda)$ are the refractive indices of the fiber core and the medium inside the cavity, respectively.

Determining amplitude spectral density $U_1(\lambda)$ is slightly more complicated than determining amplitude spectral density $U_0(\lambda)$. Apart from the Fresnel phenomenon, one should also take into account the phenomenon of diffraction causing the beam to widen inside the cavity and changing the wavefront radius of curvature of the beam, the attenuation of the beam inside the cavity, the phase shift proportional to the distance that beam propagates inside the cavity, the Gouy effect causing an additional phase shift of the beam, $\zeta_1(\lambda)$, and coupling of the beam coming out of the cavity with the beam propagating in the core of the optical fiber. Taking all these phenomena into account, $U_1(\lambda)$ can be determined as

$$U_1(\lambda) = t_{12}(\lambda)r_{23}(\lambda)t_{21}(\lambda)\sqrt{T_{\text{cav}}(\lambda)}\exp\left(-j\frac{4\pi L n_{\text{cav}}(\lambda)}{\lambda}\right)\exp\left[j\zeta_1(\lambda)\right]c_1(\lambda)U_{\text{in}}(\lambda), \tag{5}$$

where $t_{12}(\lambda)$ and $t_{21}(\lambda)$ are the complex amplitude transmittances at the interface between the optical fiber and the cavity from the optical fiber to the cavity and from the cavity to the optical fiber, respectively:

$$t_{12}(\lambda) = 1 + r_{12}(\lambda), \tag{6}$$

$$t_{21}(\lambda) = 1 - r_{12}(\lambda). \tag{7}$$

$T_{\text{cav}}(\lambda)$ is the power transmittance in the cavity at the distance of $2L$:

$$T_{\text{cav}}(\lambda) = \exp\left[-2L\mu_{\text{a}}(\lambda)\right], \tag{8}$$

where L is the length of the cavity, $\mu_a(\lambda)$ and $n_{\text{cav}}(\lambda)$ are the absorption coefficient and the refractive index of the medium that fills the cavity, respectively, and $c_1(\lambda)$ is the complex coupling

coefficient of the beam coming out of the cavity with the beam propagating in the core of the optical fiber which includes a mismatch of diameters of beams outgoing from the cavity and propagating in the core of the optical fiber and curvatures of the wavefronts of these beams.

For a step-index single-mode optical fiber, the beam propagating inside the cavity can be approximated by a Gaussian beam for which [33]

$$\exp\left[j\zeta_1(\lambda)\right] c_1(\lambda) = \frac{2\pi n_{\text{cav}}(\lambda) w_0^2(\lambda)}{2\pi n_{\text{cav}}(\lambda) w_0^2(\lambda) - j2L\lambda}, \tag{9}$$

where $w_0(\lambda)$ is the fundamental mode field radius and L is the cavity length.

By substituting (3) and (5) into (2), we finally obtain

$$P_{\text{out}}(\lambda) = P_0(\lambda) + P_1(\lambda) + 2\sqrt{P_0(\lambda)P_1(\lambda)}\cos\left[\Delta\varphi(\lambda)\right], \tag{10}$$

where:

$$P_0(\lambda) = |U_0(\lambda)|^2 = R_{12}(\lambda)P_{\text{in}}(\lambda) \tag{11}$$

and

$$P_1(\lambda) = |U_1(\lambda)|^2 = R_{23}(\lambda)\left[1 - R_{12}(\lambda)\right]^2 T_{\text{cav}}(\lambda)\frac{\left[2\pi n_{\text{cav}}(\lambda) w_0^2(\lambda)\right]^2}{\left[2\pi n_{\text{cav}}(\lambda) w_0^2(\lambda)\right]^2 + (2L\lambda)^2} P_{\text{in}}(\lambda) \tag{12}$$

are the power spectral densities of the beams that are reflected at the interface between the optical fiber and the cavity and the interface between the cavity and the medium behind the cavity, respectively, $R_{12}(\lambda)$ and $R_{23}(\lambda)$ are the power reflectances ($R_{12}(\lambda) = |r_{12}(\lambda)|^2$ and $R_{23}(\lambda) = |r_{23}(\lambda)|^2$), $P_{in}(\lambda)$ is power spectral density of the beam incident on the cavity and

$$\Delta\varphi(\lambda) = \varphi_1(\lambda) - \varphi_0(\lambda) \tag{13}$$

is the phase difference between the phase shifts of the beams reflected at the interfaces between the cavity and the medium behind the cavity, $\varphi_1(\lambda)$, and between the optical fiber and the cavity, $\varphi_0(\lambda)$, relative to the incident beam phase.

If $n_1 > n_{\text{cav}}$, $\varphi_0(\lambda) = 0$, otherwise $\varphi_0(\lambda) = \pi$. The phase shift $\varphi_1(\lambda)$ is the sum of the phase shift associated with covering the distance in the cavity by the beam, $\varphi_{1L}(\lambda) = 2\pi L n_{\text{cav}}(\lambda)/\lambda$, the phase shift associated with the reflection, $\varphi_{1R}(\lambda)$, and the total shift associated with the coupling and the Gouy effect, $\varphi_{1cG}(\lambda)$ (i.e. $\varphi_{1cG}(\lambda)$ includes the phase shift caused by the curvature of the wavefront of the beam outgoing from the cavity, $\varphi_{1c}(\lambda)$, and the phase shift caused by Gouy effect, $\varphi_{1G}(\lambda)$: $\varphi_{1cG}(\lambda) = \varphi_{1c}(\lambda) + \varphi_{1G}(\lambda)$. $\varphi_{1R}(\lambda) = 0$, if $n_{\text{cav}} > n_3$ or $\varphi_{1R}(\lambda) = \pi$, if $n_{\text{cav}} < n_3$. The phase shift $\varphi_{1cG}(\lambda)$ we can obtain as the argument of the right side of (9):

$$\varphi_{1\text{cG}}(\lambda) = \arg\left[\frac{2\pi n_{\text{cav}}(\lambda) w_0^2(\lambda)}{2\pi n_{\text{cav}}(\lambda) w_0^2(\lambda) - j2L\lambda}\right] = \arctan\left[\frac{2L\lambda}{2\pi n_{\text{cav}}(\lambda) w_0^2(\lambda)}\right]. \tag{14}$$

As the Rayleigh range of the Gaussian beam inside the cavity is

$$z_0(\lambda) = \frac{\pi n_{\text{cav}}(\lambda) w_0^2(\lambda)}{\lambda}, \tag{15}$$

the relationship (14) can be rewritten as:

$$\varphi_{1\text{cG}}(\lambda) = \arctan\left[\frac{L}{z_0(\lambda)}\right]. \tag{16}$$

In a special case, when $n_1 > n_{\text{cav}}$ and $n_{\text{cav}} < n_3$, from (13) we obtain

$$\Delta\varphi(\lambda) = 2\pi L n_{\text{cav}}(\lambda)/\lambda + \pi + \arctan\left[\frac{L}{z_0(\lambda)}\right]. \tag{17}$$

Note that the total phase shift associated with the coupling and the Gouy effect, $\varphi_{1cG}(\lambda) = \arctan[L/z_0(\lambda)]$, is smaller than the phase shift caused only by the Gouy effect, $\varphi_{1G}(\lambda) = \arctan[2L/z_0(\lambda)]$.

2.2. Using sensors in the sensor network

The key aspect of using a given type of sensor to build a sensor network is the separation of measurement signals derived from individual sensors so that signals from one sensor do not interfere with signals from other sensors. One of the most frequently used signal separation methods in networks is based on wavelength-division multiplexing of the optical signal. Each sensor modulates the transmission of radiation in a narrow wavelength band with a different center wavelength. This method is applied *e.g.* in sensor networks using Bragg gratings. Another well-known signal separation method is the use of measurement of the time of flight of optical signals from the radiation source to sensors and back by the *optical time-domain reflectometry* (OTDR) or *frequency-domain reflectometry* (OFDR) systems [35, 36]. The mentioned systems are applied in intensity modulation fiber-optic sensor networks.

Since low-coherence interferometric sensors with extrinsic Fabry–Pérot cavities modulate the power of the optical signal over a very wide range of wavelengths, more advanced methods are needed to separate the signals from these sensors connected to the sensor network than the methods used in the sensor networks mentioned above. The problem is that any sensor using the Fabry–Pérot cavity modulates the signal over the entire wavelength range of the radiation source used in the sensor network which does not allow for the separation of signals from individual sensors with the use of narrowband optical filters or signal analysis from an optical spectrum analyzer measuring the level and position of spectral lines of the optical signal at the output of a sensor network (as is the case in sensor networks using *e.g.* Bragg gratings). The fact that the spectrum modulation rate changes with cavity length (see (10), (13), and (17)) can be used to separate the measurement signals derived from individual low-coherence interferometric sensors with extrinsic Fabry–Pérot cavities. For example, Fig. 2a and 2b presents examples of calculated power spectrum densities at the output of sensors that use an empty cavity formed by two end surfaces of single-mode type SMF-28 optical fibers (a refractive index of the core equal to 1.452, core diameter equal to 8.2 μm, and mode field diameter equal to 9.2 μm at 1290 nm [37, 38]) for a cavity length of 126 μm and 460 μm. It was assumed that the profile of the radiation beam coming from the optical fiber can be approximated by a Gaussian beam with the waist diameter equal to the fundamental-mode size width [33, 39]. This diameter is equal to 8.5 μm at 1290 nm which is less than the mode field diameter (provided by manufacturers of optical fibers according to the Petermann II mode field diameter definition). In calculations, it was assumed that the sensors were excited by the radiation source having a Gaussian spectrum distribution with a central wavelength $\lambda_0 = 1290$ nm and a spectral width $\Delta\lambda = 50$ nm at FWHM. The densities and their Fourier transforms are shown in Fig. 2c and 2d.

Each Fourier transforms shown in Fig. 2c and 2d has two components: the first component depends on the spectrum of the radiation source only, while the second one depends on both: the spectrum of the radiation source and the spectrum modulation rate. In sensor networks, the latter component can be used to measure changes in the length of the cavity on the basis of which

Metrol. Meas. Syst., Vol. 28 (2021), No. 2, pp. 289–305
DOI: 10.24425/mms.2021.136608

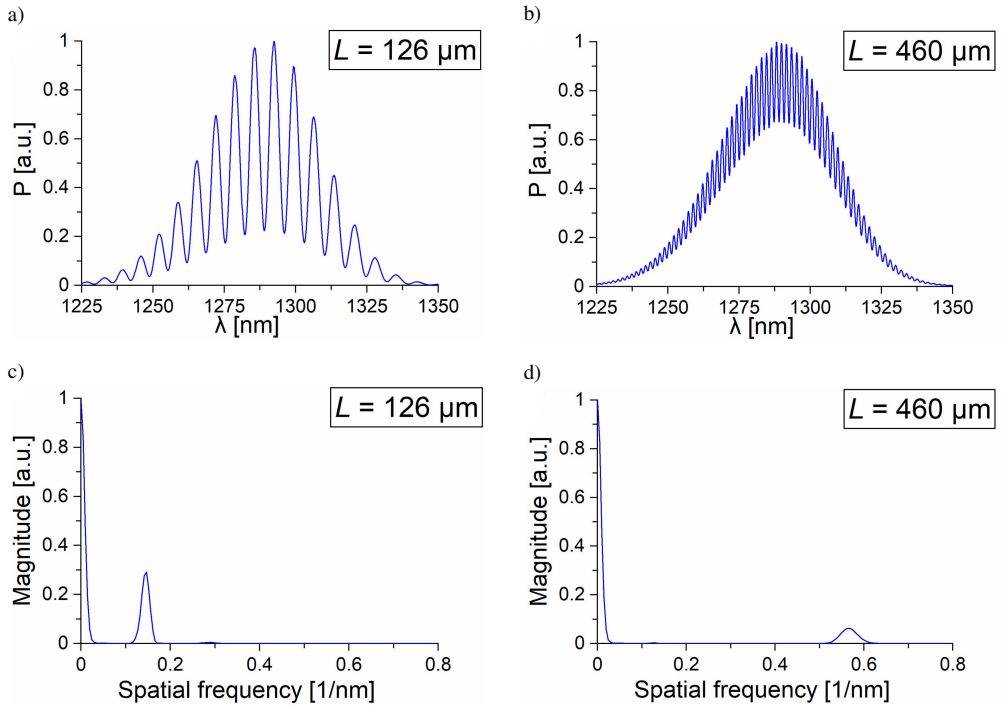

Fig. 2. Calculated power spectral densities at the output of sensors and the Fourier transforms of these power spectral densities. It was assumed that the sensors use an empty cavity formed by two end surfaces of single-mode type SMF-28 optical fibers for a cavity length of 126 µm (a) and 460 µm (b), and the radiation source has a Gaussian spectrum distribution with the central wavelength $\lambda_0 = 1290$ nm and spectral width at FWHM $\Delta\lambda = 50$ nm. The Fourier transforms of calculated power spectrum densities for a cavity length of 126 µm and 460 µm are shown in Fig. (c) and (d), respectively.

the measured quantity is measured. In the case of multiple sensors, these components could be separated by filtering if they do not overlap. Assuming the Gaussian distribution of the radiation source and assuming the same distributions of beams reflected from the cavity (with the accuracy of a constant factor) and also assuming that the phase shift $\Delta\varphi(\lambda)$ is proportional to the length of the cavity (by neglecting the Gouy effect – see (17)), the dispersion of the glass from which the optical fiber is made, and the mode field diameter dependence on the wavelength), it can be shown from (10) that it is possible to filter the above-mentioned components if the minimum difference in the length of the cavities of individual sensors, $\Delta L_{\min}$, satisfies the relationship [40, 41]:

$$\Delta L_{\min} = \frac{2 \cdot \ln 2}{\pi} \frac{\lambda_0^2}{\Delta\lambda} . \tag{18}$$

It was assumed in (1) that individual components of the Fourier transform can be separated if they are separated by a value equal to at least their length. In practice, to avoid crosstalk between signals coming from individual sensors, having different signal levels, and taking into account neglected effects when determining the relationship (18), the differences in the length of the cavities of individual sensors should be minimum twice the calculated value $\Delta L_{\min}$. For example, for $\lambda_0 = 1290$ nm and $\Delta\lambda = 50$ nm, from (18) we obtain $\Delta L_{\min} = 14.7$ µm which means that the differences in lengths of the cavities of individual sensors in the sensor network

should be not smaller than approximately 30 μm. If we assume that the shortest Fabry–Pérot cavity length should exceed 30 μm (*i.e.* so that main spectrum components can be separated from the constant component resulting from the Fourier transform – see Fig. 2c), and the longest should not exceed *e.g.* 0.5 mm (the maximum length of the cavity depends on many factors, including the resolving power measurement of the spectrum and the adopted required depth of spectrum modulation), we obtain that the maximum number of sensors connected in the network is 16. This number is directly proportional to the spectrum width of the broadband light source to be used. The 50 nm width of light results from available, relatively cheap broadband sources using super luminescence diodes. If it is necessary to build a network consisting of a greater number of sensors, sources using several super luminescence diodes with different central wavelengths, or much more expensive sources using the generation of supercontinuum or broadly tunable lasers can be used. The latter two types of sources are available and widely used in frequency-domain optical coherence tomography (FD-OCT) [42–44].

3. Experiment

The design of a low-coherence interferometric sensor with extrinsic Fabry–Pérot cavity length-based addressing is schematically shown in Fig. 3. In this construction, the first interferometer mirror is the polished end face of the single-mode SMF-28 optical fiber, ended with FC/PC connector. The second mirror is the end face of the single-mode SMF-28 optical fiber which is placed in a flat polished ferrule. Both mirrors are positioned by using a brass sleeve. Another advantage of such a solution is the possibility to change the Fabry–Pérot cavity length through the spreading or narrowing of mirrors relative to each other. However, due to the design difficulties related mainly to problems in carrying out an accurate reference measurement of the Fabry–Pérot cavity length, significantly different cavity length were set for both sensors, despite calculating the minimum difference at 30 μm.

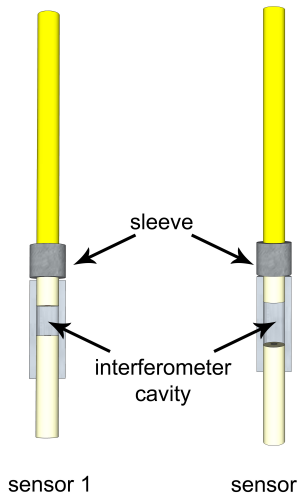

Fig. 3. The idea of a low-coherence interferometric sensor with extrinsic Fabry–Pérot cavity length-based addressing.

The sensor was designed for temperature measurements. The thermal expansion coefficients of ferrules and sleeves are about $0.5 \cdot 10^{-6}/°\mathrm{C}$ and $17 \cdot 10^{-6}/°\mathrm{C}$, respectively. Since the thermal

expansion coefficients of ferrules and optical fibers are relatively very small and very similar, the cavity length changes due to temperature change primarily depended on the linear thermal expansion of the sleeves. On the other hand, athe high difference in thermal coefficients of ferrules and the sleeve can cause a mutual shift of these elements as a result of stress caused by temperature changes. However, as the experiments showed (see Section 4), the measurements are repeatable, therefore, the mentioned shift can be neglected.

Assuming no shift between the ferrule and the sleeve, and a very little thermal expansion coefficient of the ferrule (negligible in comparison to thermal expansion coefficient of the sleeve), the length change of the cavity ΔL is a product of the air gap length L_0 (that can be bigger than the Fabry–Pérot cavity length due to cut edges of the front faces of ferrules) and the thermal expansion coefficient of the sleeve α:

$$\Delta L = L_0 + \alpha \cdot T\,, \tag{19}$$

where T is a temperature.

4. Sensor network

4.1. Network topology

Several network topologies can be applied to optical fiber-based sensor networks. The most popular ones are a bus, a dual bus (also called a ladder), and a star. In this work, we proposed a sensor network using the star topology. The easiest way to create such a network is to couple N sensors with a $1 \times N$ fiber-optic coupler. For an ideal star-topology sensor network, the power of the light source is divided into each of the sensors in ratio $1/N$ (when the coupler splits the power evenly). If needed, the optical power for each sensor can be adjusted using couplers with different couple ratios r. The star topology has an important advantage – new sensors can be added or removed without disturbing the sensors, making the network easy to scale. Also, if one sensor breaks down, it does not affect other sensors.

The use of couplers in the network allows for far-reaching network optimization from the point of view of the level of the received signal from individual sensors, *e.g.* couplers with a division different than 50 : 50 can be used. The use of couplers, although it complicates the construction of the network, is particularly beneficial if individual sensors show large losses (that is, if the sum of the power of radiation reflected from and transmitted by the Fabry–Pérot interferometer and then transmitted in the core of the optical fiber is much smaller than the power of radiation falling on the interferometer). It can take place, *e.g.*, if the cavity length is greater than the Rayleigh range of the beam subject to the phenomenon of diffraction inside the interferometer cavity. In such case, big losses result from the fact that part of the radiation power instead of further propagation in the fiber core is lost in the cavity. The phenomenon of diffraction and its consequences can be omitted in sensors with very short cavities (*i.e.* shorter than the Rayleigh range). In this situation, it is possible to build a quasi-assembled sensor consisting of a series of fiber optic-wire cells.

In general, it can be said that the design of networks consisting of low-coherence fiber optic sensors using external Fabry–Pérot interferometers is much more difficult, especially in relation to networks consisting of sensors with Bragg networks. The latter can be designed to have very low losses. Moreover, they show very selective reflection for radiation of a specific wavelength (for which Bragg condition is met) and very high transmission for other wavelengths. Radiation that has not been reflected from the Bragg grating can be used for other sensors with another fixed network in the Bragg grating. Such possibilities are not provided by low-coherence fiber

optic sensors with Fabry–Pérot interferometer, where the reflected and transmitted radiation is modulated over the entire spectrum of the radiation source and which often show much higher losses.

The output signal is a superposition of the signals from each sensor in the network. Therefore, a crucial thing is to keep the sensor signal modulated individually for each network component. If not, signal recovery from a particular sensor will be impossible.

4.2. Measurement setup

To experimentally prove the idea of a low-coherence fiber-optics sensors network, a dedicated laboratory setup was built. The setup consists of two low-coherence sensors (described in Section 3) for temperature measurements, whose cavities were equal to 126 μm and 460 μm, a superluminescent diode (S1300-G-I-20 by Superlum, Ireland), and an optical spectrum analyzer (AQ6319 by ANDO, Japan), all connected with the 2×2 single-mode fiber coupler (coupling ratio 50 : 50). Moreover, a temperature calibrator (ETC-400A by Ametek, USA) was used for temperature changes. It ensures high-temperature stability at the level of ±0.15 °C (application note [45]). The sensors of the developed network are completely independent, that is, they allow the simultaneous measurement of two different temperatures. The measurement setup is presented in Fig. 4.

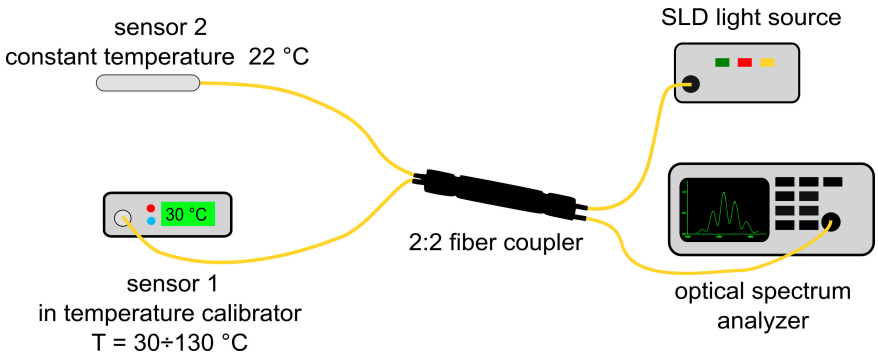

Fig. 4. Measurement setup.

The optical spectrum analyzer could be replaced by a much faster and cheaper optical spectrometer, using a diffraction grating and a CCD or CMOS detector matrix. Such a solution reduces the data acquisition time up to 5 orders of magnitude. A similar approach is applied in spectral domain optical coherent tomography (SD-OCT) systems, where it enables data acquisition at a frequency of tens of kilohertz. Unfortunately, because of the number of detector pixels, the spectral resolution of such a solution is lower than the spectral resolution of an optical spectrum analyzer. For now, the most promising way to reduce the cost of the setup and keep the high precision and resolution of the measurement seems to be the use of the tunable laser.

For verification of the operation of the sensor network, several measurements have been taken. It had been decided, that during the experiment, one of the sensors was kept at the constant temperature of 22 °C, while the temperature of the other sensor was increased and decreased in the range from 30 °C to 130 °C, with 10 °C steps. The measurement signal from both sensors was registered at the same time and on one interferogram. Selected interferograms acquired during the measurements are presented in Fig. 5 as an example.

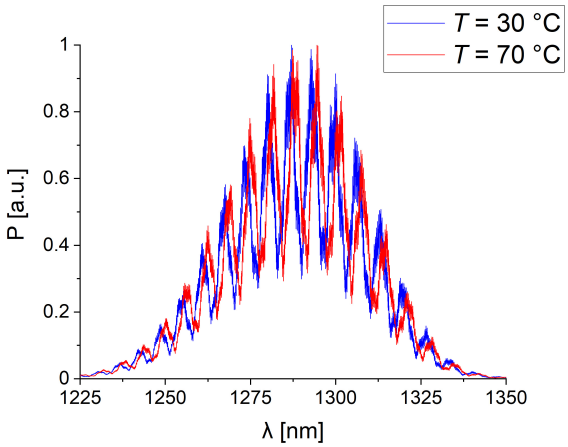

Fig. 5. Registered interferograms for temperatures equal to 30 °C and 70 °C for the sensor 1 heating cycle.

As shown, the interferograms acquired for a different temperature of at least one sensor vary. Nevertheless, it is hard to extract information about the temperature for individual sensors of the network. Thus, advanced signal processing is required.

4.3. Signal analysis

For the signal analysis, the Fourier transformation was employed. This operation enables to separate signals from both sensors connected in the network. The selected interferogram acquired during the measurements and its Fourier transform are presented in Fig. 6.

For each acquired interferogram, the Fourier transform was calculated using the MATLAB built-in *fft*( ) function. The acquired interferogram was padded with trailing zeros to length 2048, and then Fourier transform was calculated. Since the SLD source has Gaussian spectral characteristics, no windowing function was applied. As shown in Fig. 6b, the Fourier transform of the acquired signal consists of the component depending on the spectrum of the radiation source only (the DC component with a spatial frequency close to 0) and components depending on both the spectrum of the radiation source and the spectrum modulation rate (the sensor components). Due to the selected parameters of sensor cavities lengths, the sensor components of the spectrum are well separated in the spatial frequency domain. The main spectrum component from sensor 1 is marked with the black arrow, whereas the main spectrum component from sensor 2 is marked with the red arrow in Fig. 6b.

To obtain information about the spectrum fringes separation, the inverse Fourier transform of the signal components was employed. The inverse Fourier transform was calculated using the MATLAB built-in *ifft*( ) function. The length of the computed interferogram was kept the same as the length of the acquired interferogram, *i.e.*, equal to 2001. For each sensor, only the main components were taken into account. Also, the DC component was omitted because of the impossibility of its separation. Due to that, the shape of the processed interferogram is quite different from the original one. The processed interferograms (for sensor 2 temperature equal to 70 °C) for both sensors are shown in Fig. 6c and 6d. For separated sensor interferograms, the number of maxima is higher for sensor 2 whose temperature is higher than for sensor 1. It is in line with our expectations – the length of the sensor 1 cavity is smaller than that of sensor 2 which

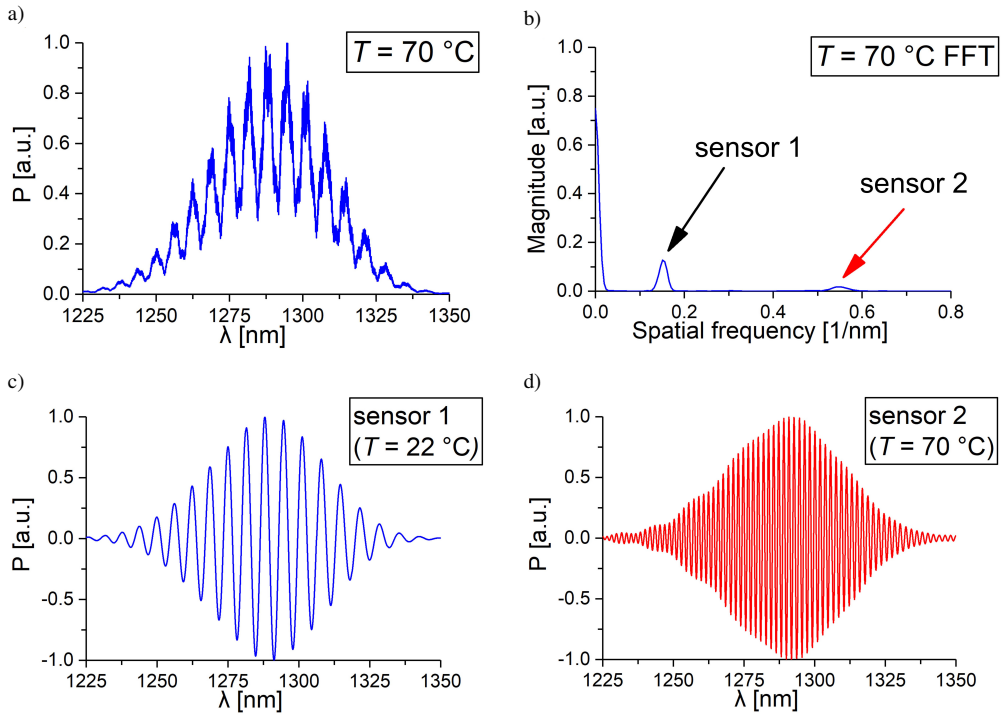

Fig. 6. Signal analysis of registered interferograms. a) Registered interferogram for the temperature of 70 °C for the sensor 1 heating cycle. b) Fourier transform of registered interferogram with components of sensors 1 and 2 marked with a black and red arrow, respectively. c) Calculated interferogram for the temperature of 70 °C for heating cycle for sensor 1. d) Calculated interferogram for the temperature of 70 °C for heating cycle for sensor 2.

influences the length of the optical path in the interferometer cavity. Therefore, for sensor 2, the number of maxima in the calculated interferogram is higher than the number of maxima in the calculated interferogram for sensor 1. Moreover, the maximum wavelength values for sensor 2 in various temperature conditions are different – the temperature is higher, the maximum wavelength is red-shifted.

4.4. Results

The analysis described in Section 4.3 was performed for each acquired interferogram, and the calculated interferograms (see Fig. 6c and 6d) were analyzed. Then, using the fitting method based on the developed software, the sensor cavity length was determined for each performed measurement.

The analysis in the function of temperature above was performed for both sensors of the network. We observed dependence between the cavity length wavelength corresponding to the obtained signal interferogram and the temperature calibrator reading. The cavity lengths of both sensors as the function of temperature are presented in Fig. 7a and 7b, respectively.

For sensor 1, we observed an increase of the calculated cavity length while temperature increased. The obtained data were fitted with a linear function with a very high determination coefficient R^2 value equal to 0.976. Apart from minor changes in the interferograms for the same

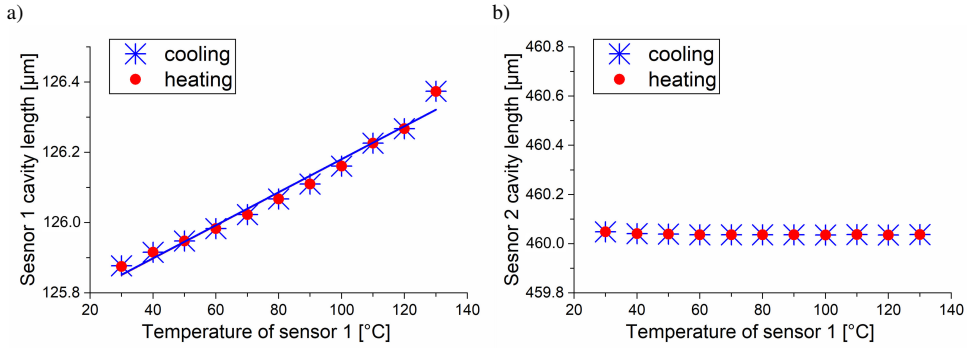

Fig. 7. Relationship between the maximum wavelength position in the function of temperature.

temperature between heating and cooling cycles, the calculated cavity length remained the same. Assuming that the output value of the system is the calculated cavity length, the slope of the characteristic (sensor temperature sensitivity) can be estimated as 4.70 nm/°C.

5. Summary

In this paper, we proposed a fiber-optic sensor network using low-coherence interferometric sensors with extrinsic Fabry–Pérot cavities. We validated the network both numerically and experimentally. The signals from individual sensors can be easily separated using a Fourier transform. The proposed solution requires only one broadband light source with wavelengths lying in the transmission band of the optical fiber. These wavelengths should be longer than the cut-off wavelength of the optical fiber. The spectrum width of this source has a significant impact on the maximum number of sensors that can be used in the network so that signals from these sensors can be separated. Theoretically, more sensors in the network could be used for a wider spectrum. So far, only models of temperature sensors have been used in the work to check the possibility of building a network of fiber optic sensors using external Fabry–Pérot cavities. For practical applications, these sensors should be miniaturized. In the miniaturized version, the use of these sensors in the network can be particularly attractive for monitoring infrastructure in the power industry (*e.g.* transmission lines or cables) due to the possibility of transmitting measurement signals over a long distance in the presence of strong electromagnetic interference. Sensors of this type can be particularly attractive if dielectrics (*e.g.* ceramics) are used instead of metal elements for their construction. Another potential application area for a network of these sensors could be the monitoring of pipelines, highways, and any other structure requiring remote measurements over long distances. After meeting the requirements for the accumulation of electrostatic charge, these sensors can also be used in mines and the petrochemical industry.

Although the described concept has been validated based on the temperature sensor network, the conclusions can be extended to networks of sensors of other physical quantities, if their operation is based on an interference sensor with Fabry–Pérot cavity.

Acknowledgements

This research work was supported by the DS program of the Faculty of Electronics, Telecommunications and Informatics, Gdańsk University of Technology, and the TASK Academic Computer Centre in Gdańsk, Poland

References

[1] Tian, J., Lu, Y., Zhang, Q., & Han, M. (2013). Microfluidic refractive index sensor based on an all-silica in-line Fabry–Pérot interferometer fabricated with microstructured fibers. *Optics Express*, *21*(5), 6633–6639. https://doi.org/10.1364/OE.21.006633

[2] Liao, C. R., Hu, T. Y., & Wang, D. N. (2012). Optical fiber Fabry–Pérot interferometer cavity fabricated by femtosecond laser micromachining and fusion splicing for refractive index sensing. *Optics Express*, *20*(20), 22813–22818. https://doi.org/10.1364/OE.20.022813

[3] Selvas-Aguilar, R., Castillo-Guzman, A., Cortez-Gonzalez, L., Toral-Acosta, D., Martinez-Rios, A., Anzueto-Sanchez, G., Duran-Ramirez, V. M., & Arroyo-Rivera, S. (2016). Noncontact Optical Fiber Sensor for Measuring the Refractive Index of Liquids. *Journal of Sensors*, *2016*, 1–6. https://doi.org/10.1155/2016/3475782

[4] Marzejon, M., Karpienko, K., Mazikowski, A., & Jędrzejewska-Szczerska, M. (2019). Fibre-optic sensor for simultaneous measurement of thickness and refractive index of liquid layers. *Metrology and Measurement Systems*, *26*(3), 561–568. https://doi.org/10.24425/mms.2019.129584

[5] Harun, S. W., Yang, H. Z., Arof, H., & Ahmad A. (2012). Theoretical and experimental studies on coupler-based fiber optic displacement sensor with concave mirror. *Optik*, *123*(23), 2105–2108. https://doi.org/10.1016/j.ijleo.2011.10.006

[6] Zhang, Q., Zhu, T., Hou, Y., & Chiang, K. S. (2013). All-fiber vibration sensor based on a Fabry–Pérot interferometer and a microstructure beam. *Journal of the Optical Society of America B, 20*(5), 1211–1215. https://doi.org/10.1364/JOSAB.30.001211

[7] Kim, D. H., Han, J. H., & Lee, I. (2005). Vibration Measurement and Flutter Suppression Using Patch-type EFPI Sensor System. *International Journal of Aeronautical and Space Sciences*, *6*(1), 17–26. https://doi.org/10.5139/IJASS.2005.6.1.017

[8] Jiang, M., & Gerhard, E. (2001). A simple strain sensor using a thin film as a low-finesse fiber-optic Fabry–Pérot interferometer. *Sensors and Actuators A: Physical*, *88*(1), 41–46. https://doi.org/10.1016/S0924-4247(00)00494-5

[9] Yang, F., Wang, Z. K., & Wang, D. N. (2019). A highly sensitive optical fiber strain sensor based on cascaded multimode fiber and photonic crystal fiber. *Optical Fiber Technology*, *47*, 102–106. https://doi.org/10.1016/j.yofte.2018.11.029

[10] Dai, L., Wang, M., Cai, D., Rong, H., Zhu, J., Jia, S., & You, J., (2013). Optical Fiber Fabry–Pérot Pressure Sensor Based on a Polymer Structure. *IEEE Photonics Technology Letters*, *25*(24), 2505–2508. https://doi.org/10.1109/LPT.2013.2287289

[11] Du, Y., Qiao, X., Rong, Q., Yang, H., Feng, D., Wang, R., Hu, M., & Feng, Z. (2014). A Miniature Fabry–Pérot Interferometer for High Temperature Measurement Using a Double-Core Photonic Crystal Fiber. *IEEE Sensors Journal*, *14*(4), 1069–1073. https://doi.org/10.1109/JSEN.2013.2286699

[12] Zhao, Y., Zhao, J., & Zhao, Q. (2020). High sensitivity seawater temperature sensor based on no-core optical fiber. *Optical Fiber Technology*, *54*. https://doi.org/10.1016/j.yofte.2019.102115

[13] Xu, W., Huang, W.-B., Huang, X.-G., & Yu, C. (2013). A simple fiber-optic humidity sensor based on extrinsic Fabry–Pérot cavity constructed by cellulose acetate butyrate film. *Optical Fiber Technology*, *19*(6), 583–586. https://doi.org/10.1016/j.yofte.2013.09.005

[14] Lv, R.-Q., Zhao, Y., Wang, D., & Wang, Q. (2014). Magnetic Fluid-Filled Optical Fiber Fabry–Pérot Sensor for Magnetic Field Measurement. *IEEE Photonics Technology Letters*, *26*(3), 217–219. https://doi.org/10.1109/LPT.2013.2290546

[15] Wang, W., & Li, F., (2014). Large-range liquid level sensor based on an optical fibre extrinsic Fabry–Pérot interferometer. *Optics and Lasers in Engineering*, *52*, 201-205. https://doi.org/10.1016/j.optlaseng.2013.06.009

[16] Lu, Y., Li, H., Qian, X., Zheng, W., Sun, Y., Shi, B., & Zhang Y. (2020). Beta-cyclodextrin based reflective fiber-optic SPR sensor for highly-sensitive T detection of cholesterol concentration. *Optical Fiber Technology*, *56*, 102187-1-6. https://doi.org/10.1016/j.yofte.2020.102187

[17] Huang, Y. W., Tao, J., & Huang, X. G. (2016). Research Progress on F-P Interference–Based Fiber-Optic Sensors. *Sensors (Switzerland)*, *16*(9), 1424. https://doi.org/10.3390/s16091424

[18] Perez-Herrera, R. A., & Lopez-Amo, M. (2013). Fiber optic sensor networks. *Optical Fiber Technology*, *19*(6), 689-699. https://doi.org/10.1016/j.yofte.2013.07.014

[19] Lönnermark, A., Hedekvist, P. O., & Ingason, H. (2008). Gas temperature measurements using fibre Bragg grating during fire experiments in a tunnel. *Fire Safety Journal*, *43*(2), 119–126. https://doi.org/10.1016/j.firesaf.2007.06.001

[20] Huang, Y., Fang, X., Bevans, W. J., Zhou, Z., Xiao, H., & Chen, G. (2013). Large-strain optical fiber sensing and real-time FEM updating of steel structures under the high temperature effect. *Smart Materials and Structures*, *22*(1). https://doi.org/10.1088/0964-1726/22/1/015016

[21] Kersey, A. D. (1996). A Review of Recent Developments in Fiber Optic Sensor Technology. *Optical Fiber Technology*, *2*(3), 291–317. https://doi.org/10.1006/ofte.1996.0036

[22] Márquez-Cruz, V. A., & Hernández-Cordero, J. A. (2014). Fiber optic Fabry–Pérot sensor for surface tension analysis. *Optics Express*, *22*(3), 3028–3038. https://doi.org/10.1364/OE.22.003028

[23] Jędrzejewska-Szczerska, M. (2014). Response of a New Low-Coherence Fabry–Pérot Sensor to Hematocrit Levels in Human Blood. *Sensors (Switzerland)*, *14*(4), 6965–6976. https://doi.org/10.3390/s140406965

[24] Li, M., Wang, S., Jiang, J., Liu, K., Yu, L., & Liu, T. (2020). Cryogen adaptive and integrated differential pressure sensor for level sensing based on an optical Fabry–Pérot interferometer. *Applied Optics*, *59*(8), 2457–2461. https://doi.org/10.1364/AO.384293

[25] Zhang, X., Wang, W., Chen, H., Tang, Y., Ma, Z., & Wang, K. (2019). Two-Parameter Elliptical Fitting Method for Short-Cavity Fiber Fabry–Pérot Sensor Interrogation. *Sensors (Switzerland)*, *19*(1), 36-1–11. https://doi.org/10.3390/s19010036

[26] Wei, H., & Krishnaswamy, S. (2020). Adaptive fiber-ring lasers based on an optical fiber Fabry–Pérot cavity for high-frequency dynamic strain sensing. *Applied Optics*, *59*(2), 530–535. https://doi.org/10.1364/AO.377368

[27] Maciak, E. (2019). Low-coherence Interferometric Fiber Optic Sensor for Humidity Monitoring Based on Nafion®Thin Film. *Sensors (Switzerland)*, *19*(3). https://doi.org/10.3390/s19030629

[28] Liu, Y., & Qu, S. (2014). Optical fiber Fabry–Pérot interferometer cavity fabricated by femtosecond laser-induced water breakdown for refractive index sensing. *Applied Optics*, *53*(3), 469-474. https://doi.org/10.1364/AO.53.000469

[29] Nespereira, M., Coelho, J. M. P., & Rebordaão, J. M. (2019). A Refractive Index Sensor Based on a Fabry–Pérot Interferometer Manufactured by NIR Laser Microdrilling and Electric Arc Fusion. *Photonics*, *6*(4). https://doi.org/10.3390/photonics6040109

[30] Yang, Y., Wang, Y., Jiang, J., Zhao, Y., He, X., & Li, L. (2019). High-sensitive all-fiber Fabry–Pérot interferometer gas refractive index sensor based on lateral offset splicing and Vernier effect. *Optik (Stuttg)*, *196*. https://doi.org/10.1016/j.ijleo.2019.163181

[31] Domínguez-Flores, C. E., Monzón-Hernández, D., Minkovich, V. P., Rayas, J. A., & Lopez- Cortes, D. (2020). In-Fiber Capillary-Based Micro Fabry–Pérot Interferometer Strain Sensor. *IEEE Sensors Journal*, *20*(3), 1343–1348. https://doi.org/10.1109/JSEN.2019.2948013

[32] Shi, Q., Lv, F., Wang, Z., Jin, L., Hu, J.J., Liu, Z., Kai, G., & Dong, X. (2008). Environmentally Stable Fabry–Pérot-Type Strain Sensor Based on Hollow-Core Photonic Bandgap Fiber. *IEEE Photonics Technology Letters*, *20*(4), 237–239. https://doi.org/10.1109/LPT.2007.913335

[33] Pluciński, J., & Karpienko, K. (2016). Fiber optic Fabry–Pérot sensors: modeling versus measurements results. *Proc. SPIE 10034, 11th Conference on Integrated Optics: Sensors, Sensing Structures, and Methods*, 100340H. https://doi.org/10.1117/12.2244578

[34] Pluciński, J., & Karpienko, K. (2016). Response of a fiber-optic Fabry–Pérot interferometer to refractive index and absorption changes: modeling and experiments. *Proc. SPIE 10161, 14th International Conference on Optical and Electronic Sensors*, 101610F. https://doi.org/10.1117/12.2247510

[35] Pluciński, J., Wierzba, P., & Kosmowski, B. B. (2005). Time-of-flight fiber optic sensors for strain and temperature measurement. *Proceedings of SPIE 5952, Optical Fibers: Applications*, 59521H. https://doi.org/10.1117/12.622880

[36] Engelbrecht, R. (2017). Fiber Optic Strain and Temperature Sensing: Overview of Principles. *B6 – Distributed and Fiber Bragg Grating Sending I, Proceedings Sensor 2017,* Germany, 255–260. https://doi.org/10.5162/sensor2017/B6.1

[37] Corning (2014). *Corning®SMF-28®Ultra Optical Fiber*. https://www.corning.com/media/worldwide/coc/documents/Fiber/SMF-28%20Ultra.pdf

[38] Thorlabs (2015). Single Mode Fiber with Ø 900 μm Hytrel Jacket – SMF-28-J9.

[39] Marcuse, D. (1977). Loss analysis of single-mode fiber splices. *The Bell System Technical Journal 56(5)*, 703–718. https://doi.org/10.1002/j.1538-7305.1977.tb00534.x

[40] Bouma, B. E., & Tearney, G. J. (2002). *Handbook of Optical Coherence Tomography*. New York: Marcel Dekker.

[41] Drexler, W., & Fujimoto, J. G. (2015). *Optical Coherence Tomography: Technology and Applications* (2nd ed.). New York: Springer International Publishing.

[42] Strąkowski, M., Pluciński, J., & Kosmowski, B. B. (2011). Polarization sensitive optical coherence tomography with spectroscopic analysis. *Acta Physica Polonica A*, *120*(4), 785–788. https://doi.org/10.12693/APhysPolA.120.785

[43] Strąkowski, M., Kraszewski, M., Trojanowski, M., & Pluciński, J. (2014). Time-frequency analysis in optical coherence tomography for technical objects examination. *Proceeding of SPIE 9132, Optical Micro- and Nanometrology V*, 91320N. https://doi.org/10.1117/12.2052142

[44] Kamińska, A. M., Strąkowski, M. R., & Pluciński, J. (2020). Spectroscopic Optical Coherence Tomography for Thin Layer and Foil Measurements. *Sensors*, *20*(19), 5653. https://doi.org/10.3390/s20195653

[45] Ametek (2020). *Temperature calibrator Ametek ETC-400A specification*. https://www.testequipmentdepot.com/ametek/temperaturecalibrator/etc400a.htm

Metrol. Meas. Syst., Vol. 28 (2021), No. 2, pp. 289–305
DOI: 10.24425/mms.2021.136608

Katarzyna Karpienko was born in Suwałki, Poland in 1987. She received a B.Sc. degree in electronic engineering and telecommunication from Gdańsk University of Technology, Gdańsk, Poland, in 2012 and an M.Sc. degree in electronic engineering and telecommunications in 2013 from the same university. In 2018, she obtained a Ph.D. in technical sciences for work in the field of fiber optic sensors. Her research is focused on the application of optical methods in medicine.

Adam Mazikowski (born in 1971) received the master's degree in Electronic Equipment Design in 1995 from Gdańsk University of Technology. In 2003 he received Ph.D. degree in optoelectronics from the Gdańsk University of Technology, Faculty of Electronics, Telecommunication and Informatics, Gdańsk, Poland. From 1995 to 2003, he was Research Assistant and since 2003, he has been Assistant Professor with the Department of Metrology and Optoelectronics, Gdańsk University of Technology, Poland. His research interests include non-contact emissivity and temperature measurement, optoelectronic sensors (incl. biomedical sensors), optoelectronic displays, photometry and colorimetry, and virtual reality systems.

Marcin J. Marzejon was born in Tczew, Poland, in 1993. He received the M.Sc. (2017) degree from Gdańsk University of Technology (GUT), Poland. In 2018, he joined the Physical Optics and Biophotonics Group at the Institute of Physical Chemistry PAS, led by prof. Maciej Wojtkowski. He is currently pursuing the Ph.D. degree in the Department of Metrology and Optoelectronics, GUT. His research activity is focused on the application of optics in biology and medicine.

Jerzy Pluciński (born in 1960) received an M.Sc. degree in electronics from the Faculty of Electronics, Gdańsk University of Technology, Poland in 1984, and then in 1994, obtained his Ph.D. degree in optoelectronics (summa cum laude). In 2010, he obtained Habilitated Doctor degree (summa cum laude) from the same university. His research interests are optoelectronics and photonics, optics of highly scattering materials, optical coherence tomography, optical fiber sensors, and laser technology. He has authored or co-authored over 150 scientific papers, 2 books, and 3 book chapters. Now he is Professor at Gdańsk University of Technology, Poland.